SOFT ROBOTICS
Volume 00, Number 00, 2020
Mary Ann Liebert, Inc.
DOI: 10.1089/soro.2020.0004

SoRo
Soft Robotics

3D Printed Biomimetic Soft Robot with Multimodal Locomotion and Multifunctionality

Erina Baynojir Joyee,[1] Adam Szmelter,[2] David Eddington,[2] and Yayue Pan[1]

Abstract

Soft robots can outperform traditional rigid robots in terms of structural compliance, enhanced safety, and efficient locomotion. However, it is still a grand challenge to design and efficiently manufacture soft robots with multimodal locomotion capability together with multifunctionality for navigating in dynamic environments and meanwhile performing diverse tasks in real-life applications. This study presents a 3D-printed soft robot, which has spatially varied material compositions (0–50% particle–polymer weight ratio), multiscale hierarchical surface structures (10 nm, 1 μm, and 70 μm features on 5 mm wide robot footpads), and consists of functional components for multifunctionality. A novel additive manufacturing process, magnetic-field-assisted projection stereolithography (M-SL), is innovated to fabricate the proposed robot with prescribed material heterogeneity and structural hierarchy, and hence locally engineered flexibility and preprogrammed functionality. The robot incorporates untethered magnetic actuation with superior multimodal locomotion capabilities for completing tasks in harsh environments, including effective load carrying (up to $\sim$30 times of its own weight) and obstacle removing (up to 6.5 times of its own weight) in congested spaces (e.g., 5 mm diameter glass tube, gastric folds of a pig stomach) by gripping or pushing objects (e.g., 0.3–8 times of its own weight with a velocity up to 31 mm/s). Furthermore, the robot footpads are covered by multiscale hierarchical spike structures with features spanning from nanometers (e.g., 10 nm) to millimeters. Such high structural hierarchy enables multiple superior functions, including changing a naturally hydrophilic surface to hydrophobic, hairy adhesion, and excellent cell attaching and growth properties. It is found that the hairy adhesion and the engineered hydrophobicity of the robot footpad enable robust navigation in wet and slippery environments. The multimaterial multiscale robot design and the direct digital manufacturing method enable complex and versatile robot behaviors in sophisticated environments, facilitating a wide spectrum of real-life applications.

Keywords: multimaterial multiscale 3D printing, drug delivery, magnetic actuation, DLP projection stereolithography

Introduction

Soft robots have significant advantages over conventional rigid robots due to their soft and compliant structure, in addition to their adaptability to sophisticated environments.[1–5] They can outperform conventional robots in terms of complex motions, adaptability, and enhanced safety for sophisticated applications. These advantages enable soft robots to have a broad scope of applications, ranging from imaging and biosensing to drug delivery and industrial implementation. In recent works, various small-scale soft robots have been demonstrated based on different actuation mechanisms,[6–8] sensing capabilities,[9,10] or targeted functionalities.[10–13] These robots generally implement morphological computation or active sensing of the surrounding environment to achieve proper dexterity and deflection to conduct a specific task. However, most of the existing small-scale soft robots demonstrated only single or bimodal locomotion, that is, less than two degrees of freedom (DOF), which limits the potential of the robot to realize high mobility in dynamic environments.

Extensive studies on soft robot have been conducted to achieve excellent locomotion capability. Most of them focused on surface rolling[11,14–16] and snake movement.[17–21]

Departments of [1]Mechanical and Industrial Engineering and [2]Bioengineering, University of Illinois at Chicago (UIC), Chicago, Illinois, USA.

For example, in the work demonstrated by Miyashita *et al.*,[11] the surface rolling is quite effective for *in vivo* applications such as wound patching in the stomach. Yim and Sitti[16] reported capsule-shaped robots that roll on the stomach surface and can perform biopsies and deliver medicine. In the work by Luo *et al.*,[17] a snake movement-inspired soft robot was demonstrated and it was capable of bending on flat surfaces with variable frictional characteristics. Recently, Kim *et al.*[22] reported a very thin, thread-like soft robot, which has omnidirectional steering and navigating capabilities based on magnetic actuation. A hydrogel skin was grown on the robot surface, significantly reducing the friction by more than 10 times during navigation.

The multifunctional soft robots and actuation strategies presented in literature face several limitations. Utilizing tethered control system makes the actuation design inefficient[1,15,23,24] and limits load-carrying capability of the soft robot.[1,15,23,25] Some untethered actuation strategies also have limited or even no obstacle-removing capability, relatively weak body support,[14,26,27] or complex assembly-based fabrication process.[15,28,29] Furthermore, harsh environments involving humidity, liquid or plasmatic mediums that incorporate a high level of friction can severely compromise the performance of soft robots.[12–14,26,27,30,31]

Several studies have worked on developing soft robots to overcome these limitations. Soft robots capable of moving efficiently on tissue surfaces and varied functional operations have been produced by investigating different actuation strategies, fabrication techniques, and materials.[10,11,16,32] Miyashita *et al.*[11,32] investigated surface rolling mechanism and demonstrated a soft robot capable of moving inside the esophagus and stomach tissue model. Kim *et al.*[33] incorporated microfiber pads into the robot's toes to enable the directional adhesion and help climbing on a smooth surface. Umedachi *et al.*[34,35] demonstrated a deformable robot, capable of crawling and steering with a reasonable speed and electrically powered SMA coils. A 3D printing technique and postmanually assembly process were used to fabricate the robot. Yang *et al.*[36,37] demonstrated hydrophobic microstructures[36–38] and Kim *et al.*[22,39] designed magnetically controlled soft matters. Additionally, some researchers,[9,22,39–41] including Diller and Sitti[40] and Kuo *et al.*,[41] designed compliant microgrippers for gripping motions, precise transport, and programmable assembly of microparts at remote environments. While recent efforts devoted to achieving excellent locomotion or producing a specific function for some advanced applications, the production of multifunctional soft robots with a high efficiency for diverse tasks in dynamic environments is still beyond current capability, mainly due to the challenges in robot design and lack of efficient multimaterial multifunctional manufacturing technologies.

In this study, a soft robot composed of elastic polymer and magnetic particles is proposed for magnetic actuation and untethered locomotion. Key novelties proposed in this study include: (1) The incorporation of the heterogeneous material composition together with the hierarchical surface structure in the robot design, which enables us to integrate multiple superior functions in a single robot; and (2) The assembly-free direct digital manufacturing method, which makes it possible to fabricate the complicated design in one piece efficiently and effectively.

The material composition of the three-dimensional (3D) robot is designed in a voxel by voxel fashion, to locally engineer its elasticity and magnetic properties, and hence to achieve multimodal locomotion and complicated actuations such as on-demand drug releasing. Bi-axial bending is enabled in the *xy* plane and *z* axis through magnetic actuation, which allows the robot to navigate inside confined spaces and complicated structures. Multimodal locomotion such as crawling, steering, turning, and underwater moving, is investigated with the multimaterial robot design. To integrate more functional characteristics, 3D hierarchical structures, including nano-sized holes, micron-sized spikes and surface wrinkles are incorporated in the millimeter-sized robot footpads. The hierarchical surface structure not only increases the directional adhesive force of the robot leg during locomotion, but also changes the wetting property of the robot leg surface from its hydrophilic nature to highly hydrophobic. Such engineered hydrophobicity allows stronger grip and adherence on both dry and wet surfaces, making the multimodal locomotion more robust. Furthermore, the wrinkled surface texture allows enhanced cell compatibility and viability. Incorporated into the footpad geometry, this unique wrinkled morphology can have great potential for cell and tissue engineering.

A novel 3D printing technique, magnetic-field-assisted projection stereolithography (M-SL), is developed to fabricate the proposed robots with freeform geometries, spatially varied material compositions, and hierarchical surface structures with features spanning from nanometers to millimeters. Using the M-SL process, the multimaterial multiscale soft robot is manufactured directly from the digital design, in one-step and one-platform, without any postprocessing or assembling procedures.

In this article, the as-fabricated soft robot prototype is tested in varied cases, including walking in a curly maze, targeted liquid/solid drug delivery in a human stomach model and in a pig stomach, crawling underwater, obstacle removing in congested spaces with a high speed, and cell seeding and growth. The enhanced functionality of the soft robot can be utilized in several applications and in this article, three such applications have been demonstrated. The first application is controlled and targeted drug delivery. The robot can carry both liquid and solid drugs to a targeted location and release on demand, navigating through dynamic environments and on different surfaces with obstacles. Hydrophobic property of the footpads becomes crucial in navigating through slippery and wet surfaces during the drug delivery application. The second demonstration is for intrabronchial applications such as removing obstacles from airways or bronchial pathways with a magnetically controlled frontal gripper attached to the anterior leg of the robot. The third application tests cell adhesion and growth on the robot footpad, demonstrating the robot's ability to facilitate cell growth and potential use for many other *in vivo* applications.

Results and Discussion

Bioinspired design of a multimaterial multiscale soft robot

The fabrication of the soft robot starts from a digital design developed in Solidworks (version 2018; Concord, MA, USA) (Fig. 1A, B). The functional parts of the robot body, including anterior and posterior legs are made of magnetic particle/polymer composite (EMG 1200 dry magnetic nanoparticles

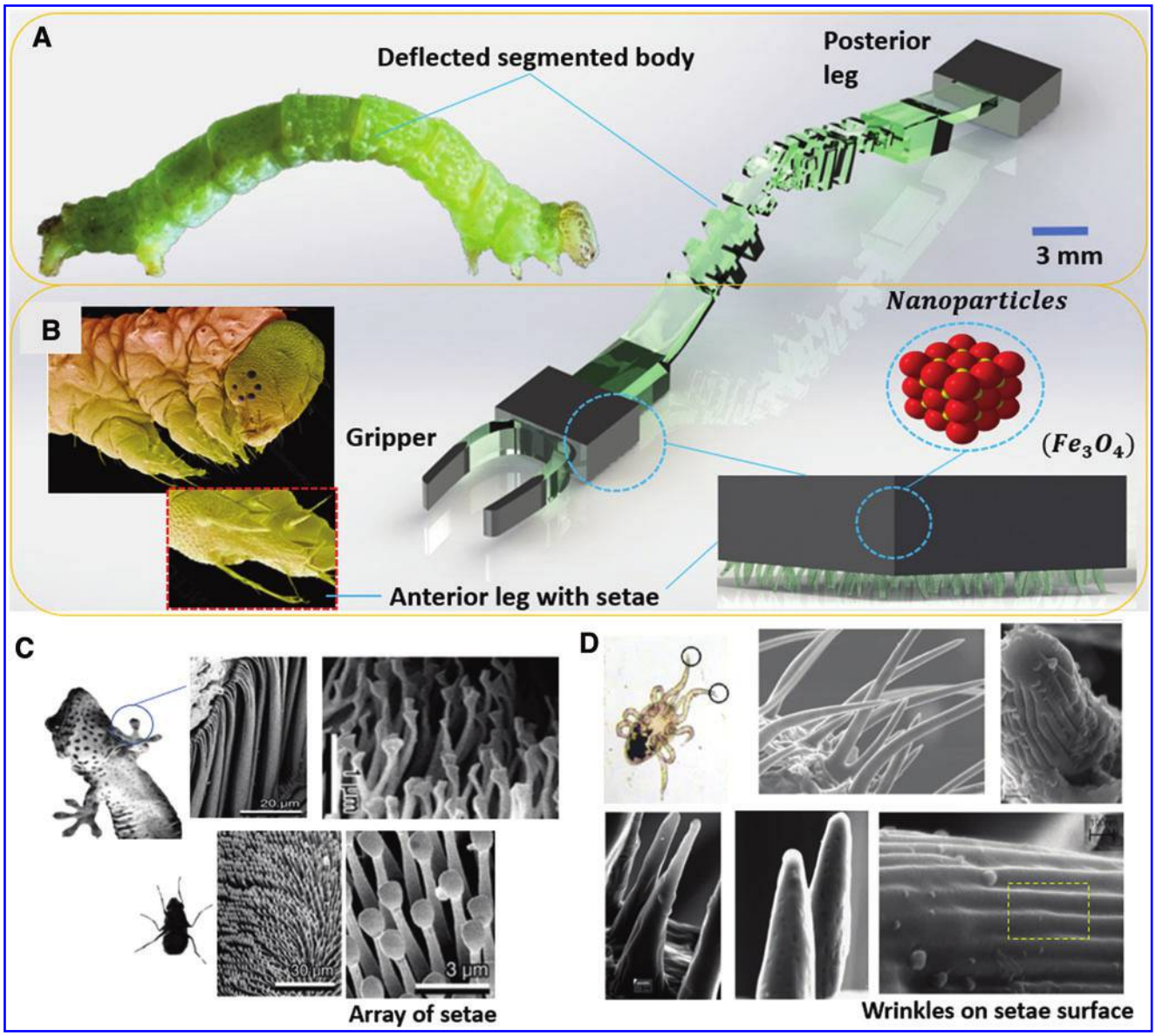

FIG. 1. Design overview of the proposed soft robot. **(A, B)** Digital model of the multimaterial soft robot with multiscale features. *Gray* color represents the magnetic particle-polymer composite and *green* represents flexible polymer. **(C)** Scanning electron microscopy images of the adhesive system of the fly ([wet fibrillar] and gecko [dry fibrillar]). Reproduced with permission.[42] Copyright 2018, Springer. **(D)** Scanning electron microscopy images of setae of *Dermanyssus gallinae* and different morphology (grooved and porous) of the seta wall. Reproduced with permission.[43] Copyright 2005, Elsevier. Color images are available online.

[Ferrotec (USA) Corporation, NH, USA]) with a 10 nm nominal particle diameter distributed in polymer resin, whereas the rest of the body is made of flexible polymer resin. The magnetic particle/polymer composite in the two legs are smart materials with preprogrammed elastic and magnetic properties. This enables the magnetic actuation of the soft robot. Additionally, the anterior leg can be integrated with a functional component designed for target applications, such as a drug-carrying reservoir or a gripper demonstrated in this study. Several design concepts of the soft robot are inspired from living organisms in nature. For example, a major design challenge in soft-bodied robots is achieving smooth multimodal locomotion in complex 3D-textured or wet slippery surface environments such as human stomach or bronchioles. The robot must be able to grip onto dynamic surfaces with low friction and high adhesion force. Thus, the surface properties of the robot legs are of utmost importance as they directly interact with biological environments. This study investigates a compliant, bioinspired footpad, which is made of biocompatible material and is covered by setae-like hierarchical surface structures to grip onto and release from a range of substrates (digital design shown in Fig. 1B).

In nature, hairy adhesive systems have evolved convergently in several animal groups. Due to their hairy adhesive micro and nanostructures (setae), these animals can walk on super slippery smooth inclined or even inverted surfaces without any contributions from their claws or legs, that is, inchworm anterior legs with setae as shown in Figure 1B. The

mechanism of adhesion with hairy adhesives is variant among different species. Some insects use fluids and capillary forces to enhance friction and adhesion,[42,44–51] whereas reptiles like *Tokay gecko* feature unique dry adhesive systems (Fig. 1C).[42,47]

When the bottom part of setae comes into contact with any substrate, shear-induced adhesion is created because of van der Waals forces at the contact point. The friction and adhesion are dependent on the number of setae and surface area that comes into contact with the underlying substrate.[44,45,47–49,52,53] Usually the orientation of setae is not perpendicular with surface but is rather sloped, which makes the structures more adaptable to different surface profiles.[44,45,53] The tapered and wrinkled setae-like structures are also observed in different arthropods like cockroaches and *Dermanyssus gallinae* (Fig. 1D),[43] which further increases the adhesion strength.

Taking inspiration from biological organisms having such tapered and wrinkled hairy setae,[43] this study investigates the design and fabrication of a soft robot with a footpad covered by multimaterial multiscale spike structures. To provide the necessary strength and compliance to sustain traction during locomotion, the spike is designed to be composed of multimaterial composites with graded particle distributions, with the highest loading fraction of particles on the spike base and the least amount of particles on the tip. Furthermore, to produce a hydrophobic surface while using hydrophilic materials, the footpad surface structure is designed to be hierarchical, with features including millimeter-sized spikes, micro-sized wrinkles on the spike surface, and nanosized pores in spike base.

As illustrated in Figure 2A, in our design, each footpad has ~1000 such multimaterial multiscale spikes. The spikes are tapered from base to tip. Figures 2E and 3E–I show the microscopic images of the 3D printed footpad and the tapered-shape spikes. Details of the fabricated micro-sized surface wrinkles and nanosized pores are discussed in the section 'Fabrication of uniform wrinkles and pores on the footpad spike structure' and are shown in Figure 3E–I. These spikes are printed using flexible resin with low elastic modulus as the base material and hence are quite flexible and very soft.

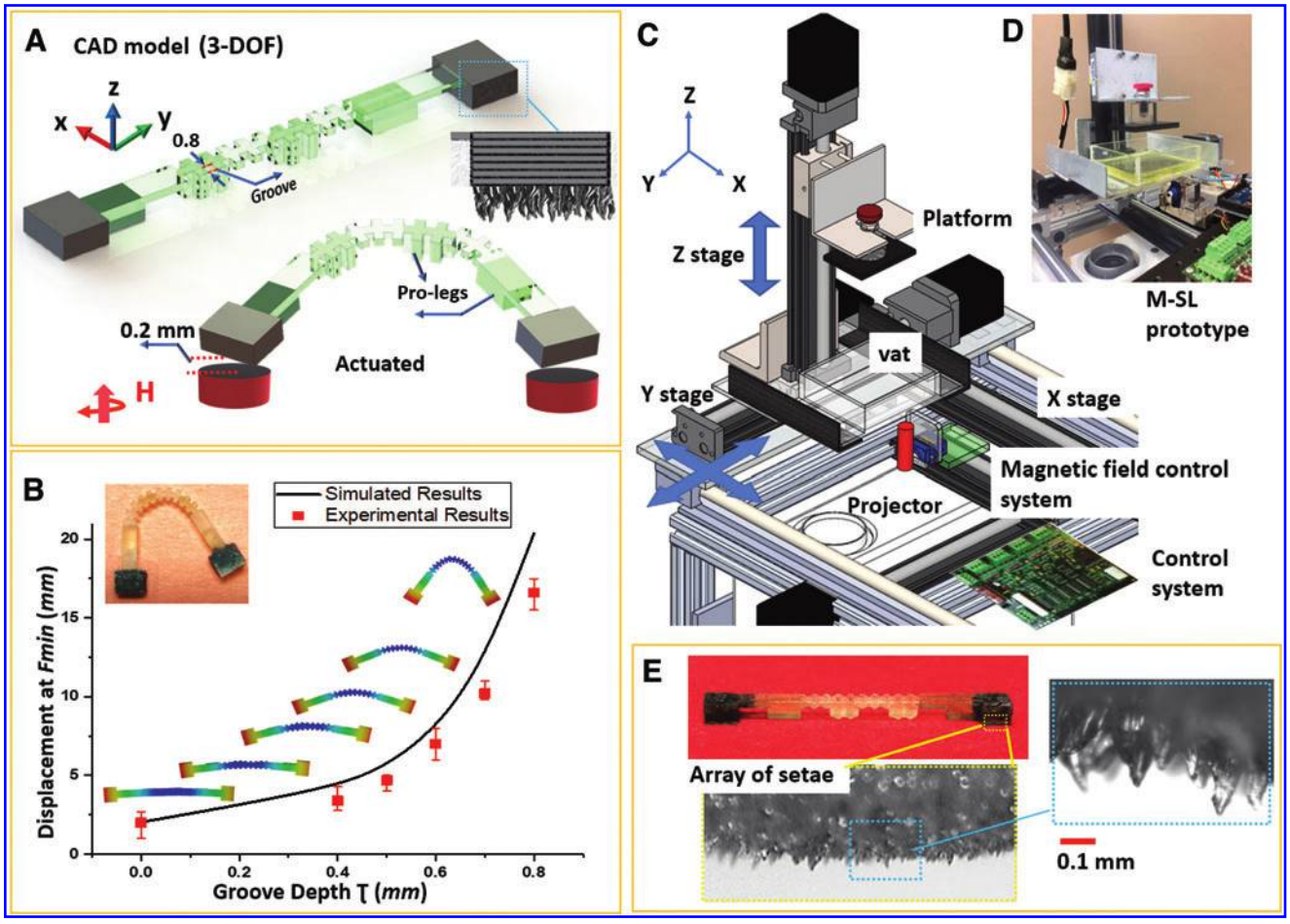

FIG. 2. Fabrication overview and characterization of the fabricated soft robot. **(A)** Schematic showing the bended robot body in the actuated state. **(B)** Comparison of the maximum displacement of the robot at $F_{min} = 0.009$ N force with different groove depth/width (T) ranging from 0 to 0.8 mm on the side wall of the robot body. The *inset* shows a 3D printed soft robot in its bended position for turning. During the turning locomotion, robot samples printed with different groove depth/width sizes (0–0.8 mm) are placed on the substrate. A permanent magnet is driven underneath the substrate to actuate the anterior leg. **(C)** Design of the M-SL testbed used to print the proposed soft robot. **(D)** M-SL prototype. **(E)** A 3D printed soft robot with hairy footpads in the anterior and posterior legs and a microscopic image of the setae-like spikes covering on the footpad surface. 3D, three-dimensional; M-SL, magnetic-field-assisted projection stereolithography. Color images are available online.

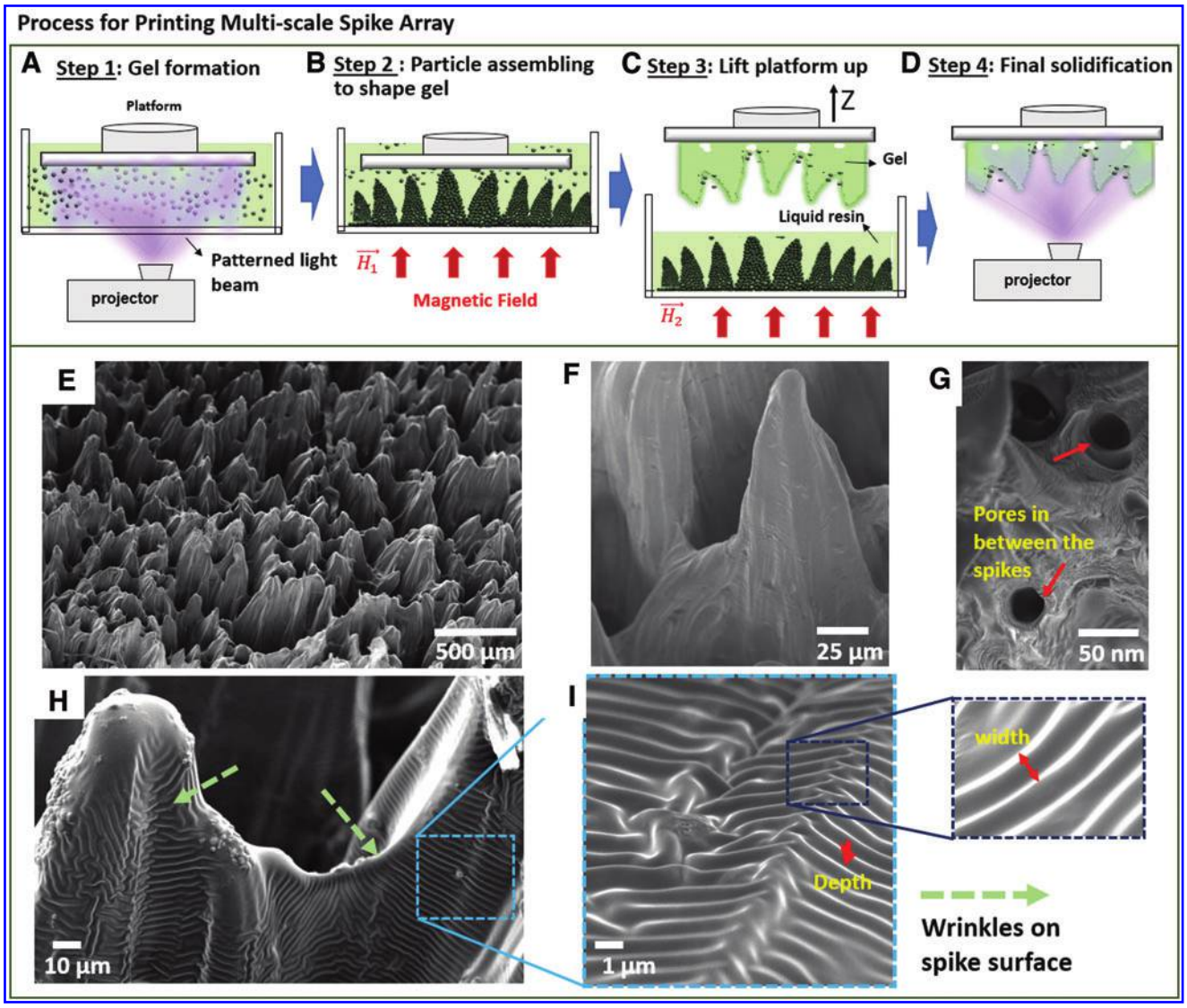

FIG. 3. Fabrication of the unique multiscale (nm–μm) surface structure. **(A–D)** Schematic of the printing process for fabricating the robot footpads with multiscale surface features ($\sim$70 μm long spikes with 5 μm diameter tip, $\sim$1 μm deep and wide wrinkles and 10–20 nm diameter pores): **(A)** Step 1: M-SL process begins by projecting light into particle resin suspension. **(B)** Step 2: An external magnetic field gradient is used to attract the magnetic particles, thus forming spikes and inducing tension on the surface of gel spike. **(C)** Step 3: Lift the platform out of the resin tank and a permanent magnet is used for removing particles in the footpad; Wrinkles and porous surface generated upon removing the particles. **(D)** Step 4: Solidification using light projection. **(E)** Scanning electron microscopy image of the tilted *top view* of the footpad; **(F)** *Side view* of one spike, and **(G)** Pores surrounded by spikes. **(H)** Wrinkles on the spike surface with consistent density. **(I)** Wrinkles are uniform regarding width and depth. Color images are available online.

When making contact with a surface (no matter smooth or rough), they are adaptable and can adjust the contact area by bending.

The digital design of the soft robot and a schematic of its footpad are shown in Figure 2A. The robot body has an overall length of 40 mm. Grooves are added in the middle section of the body for achieving 3 DOF under magnetic actuation (Fig. 2A). The total number of grooves is fixed at 10. The grooves are through cuts along z direction and designed to have the same dimension along x *and* y directions.

To achieve the highest locomotion efficiency, the groove x/y dimensions (depth/width) are optimized to achieve the maximum bending angle with respect to the applied force. Numerical and experimental analyses were conducted to test the most effective groove depth/width (τ) in the robot design (Fig. 2B). The relationship of body bending angle with the groove dimensions is characterized in COMSOL Multiphysics modeling software package (COMSOL, Inc.) using AC/DC module as a continuum model. The crawling and bending displacement was modeled in a 3D air medium with 293.15 K temperature and 1 atm environmental pressure. The local material properties of the soft robot and the underlying substrate was set manually in COMSOL material module. The objective was to see which groove depth/width could maximize the bending angle with the minimum magnetic force. For optimizing the groove depth/width, sample robots were

designed with variable depths/widths (ℸ = 0–0.8 mm). Then, forces ranging from 0.001 to 0.009 N were applied to the robot to simulate the corresponding bending shape in COMSOL. Based on the simulations, the optimized groove design had 0.8 mm depth/width along *x* and *y* directions, which leads to the maximum displacement of the robot center point from its original position, as shown in Figure 2B. Furthermore, experiments have been conducted to validate the simulation results. In our experiment, 12 robots were printed with 6 different groove depth/width (ℸ) from 0 to 0.8 mm. The maximum bending displacements were measured using a 0.009 N force for each sample with different groove size. Figure 2B shows the comparison of simulated results and experimental values. It is observed that the robot body has the maximum bending when the groove depth/width (ℸ) is 0.8 mm at 0.009 N, which is confirmed by both simulation and experimental testing. When the groove width/depth is larger than 0.8 mm, the grooves on both sides can make the middle segment of the body too narrow and fragile, thus increasing the risk of tear during turning locomotion under external force.

After the groove optimization, four regions of the robot body are extended in *z* direction to the same plane of the bottom surface of the two legs, as shown in Figure 2A. These four regions are selected to be evenly distributed along the robot body, with equivalent distance in the y direction between each of them. They are designed to mimic the pro-legs of an inchworm to improve locomotion and gripping of the substrates.

Fabrication of multimaterial soft robot with hierarchical surface structures

Figure 2C and D shows the M-SL experimental setup design and the developed prototype that was used for printing the proposed soft robot. The M-SL printing process is described in detail in the method section. Figure 2E shows the printed soft robot with footpad containing arrays of setae-like spikes. The microscopic image in the onset shows the setae-like spike surface structure in detail. Further details regarding the fabrication of footpads covered by the spike surface structures are described in the following section and illustrated in Figure 3.

The 3D printing process for printing the robot footpad with multiscale features, including tapered, wrinkled setae-like spikes with nano-sized pores is illustrated in Figure 3. In Step-1 (Fig. 3A), there is no magnetic field applied and the nanoscale spherical particles are suspended within the carrier resin evenly. The light is projected for a certain amount of time to polymerize the resin to a gel-like material in which the nanoparticles can still move freely. The relation between the curing time and formation of the gel was studied in our previous study.[54] After the gel is formed, a nonuniform magnetic field is applied from the bottom of the tank, as illustrated in Step 3. The magnetic field creates a gradient of particle assembly, within the polymer resin. This gradient rearranges the nanoparticles along the magnetic field lines. As the iron oxide nanoparticles used in this study are superparamagnetic, they have strong attraction force toward each other. This force assembles nanoparticles to micro-sized spherical clusters, which in turn grow into micro- to millimeter-sized spike structures in the resin. The final geometry of the spike is determined by the combined effect of particle size, gravitational force, surface tension, gel viscosity, and applied magnetic force.[55,56]

Fabrication of uniform wrinkles and pores on the footpad spike structure

During the formation of spikes, the microsphered nanoparticle clusters create swelling and wrinkle shapes on the polymer gel surface. Additionally, a compressive force is generated when an upward force is applied toward the gel, forming the resin gel into spike structures. This compression force follows the wrinkle lines created by microsphere clusters and increases the uniformity of wrinkle frequency on the gel surface (Fig. 3B). The wavelength of these wrinkles also depends on the diameter of the nanoparticle clusters. With the platform moving upward, the polymeric spikes are lifted out with the platform while the magneto-fluid spikes remain in the bottom of the tank. After removing the printed part from the platform, another external permanent magnet is used to pull out the rest of the magnetic particles from the swollen polymer (Fig. 3C). This relieves the stress from the surface, generating uniform wrinkles along the periphery on the surface.

In Step 4, light was projected on the surface to fully solidify the structure (shown in Fig. 3D). Upon solidification, uniaxial wrinkles on the spike surfaces become visible through electron microscopy imaging, as shown in Figure 3E–I. Nanopores are also observed in the scanning electron microscopy (SEM) image of the spikes. The overall pore size, wrinkle density, and uniformity on the spike surface can be tuned by controlling the resin and particle volume ratio, size of particles, exposure time, and applied magnetic strength. In this study, on average, the printed spikes are $\sim 70\,\mu$m long with $\sim 70\,\mu$m base diameter and $\sim 5\,\mu$m tip diameter. Each spike has uniform $\sim 1\,\mu$m wide and deep wrinkles on its surface and 10–20 nm diameter pores between spikes. The wrinkles on the tapered spike surfaces increase the intrinsic surface roughness of the footpad, and hence increase the adhesion of the robot footpad on surfaces. The study showed that the adhesion force of the spike structured footpad is $\sim 30\%$ higher compared with the measurements of the footpad without spike structure (described in Supplementary Data: Section S7). The geometry of a single spike tip and the comparison of adhesion forces between the flat footpad and footpad with spike structure are shown in Supplementary Figures S10 and S11, respectively.

The localized control of multiscale structures and materials in different segments of the footpad allows us to engineer the flexibility of the spike structure. As shown in Supplementary Figure S8, in our design, the spike tip is printed with pure flexible resin and hence is the most flexible part, while the base area that connects adjacent spikes has ~ 49 wt% iron oxide particles embedded and cured inside the polymer to make the spike strong enough to withstand any external force. The strong base and intraspike connection also help to maintain stable spacing among neighboring spikes. The material distributions in a spike tip and its surrounding base are shown in Supplementary Figure S8, where the graded distribution of iron oxide in the printed spike can be observed. The SEM images and chemical composition measurement validated that the printed spikes have the graded material composition as designed to achieve the desired flexibility at the tip region of the spikes for effective locomotion (Supplementary Movie S5).

Robot locomotion and maneuver strategy in different environments

The printed soft robot is able to navigate on different surfaces, including both liquid and solid surface, using a

combination of crawling and turning locomotion. The magnetically actuated multimodal locomotion[57] is achieved by sequential activation of magnetic forces in the posterior and anterior legs (Supplementary Data: Section S2). The applied magnetic field strength on two legs in all tests of this study was in the range of 6.5–7.8 mT, which was well under safety limit standards[58–60] and can be considered safe in a controlled environment. The soft compliant body allows biaxial bending capability, with a maximum 5.5 mm bending displacement in z axis (≈2.8 times of its own height) and 146° turning capability in the xy plane (Supplementary Data: Section S2 and Supplementary Figs. S2 and S3). This allows the robot to maneuver in enclosed spaces with multiple DOF. Figure 4A illustrates the robot's locomotion through a congested and curved maze (Supplementary Movie S1). The arc length of the curly maze was 685.8 mm long, 5 mm wide, and it had sharp turns with a maximum of 180°. The robot was able to walk through the maze (685.8 mm distance) with an average speed of 2.2 mm/s. To further show its robust and dynamic ability, the robot locomotion on a chicken skin surface at room temperature is demonstrated (Fig. 4B). The uneven rough, sticky, and wet properties of the skin surface increased the friction on the robot legs, but the robot was still able to navigate through crawling and bending (Supplementary Movie S2).

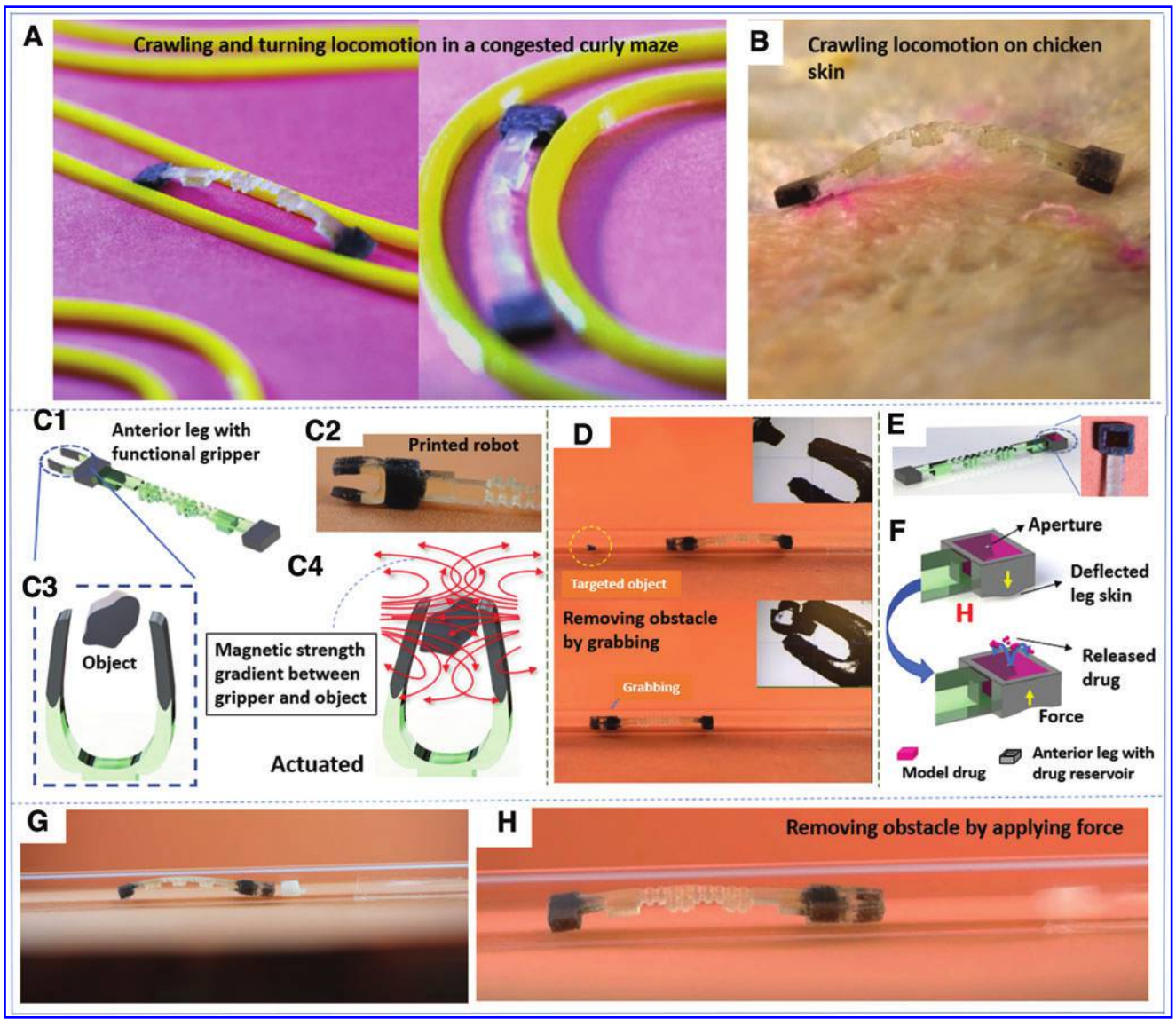

FIG. 4. Robot locomotion and integrated functional components. **(A)** Locomotion of the soft robot inside a confined space on a planar surface. **(B)** Locomotion on an *in vitro* chicken skin surface. The skin is wet and sticky which creates high friction. **(C1, C2)** Schematic and real-life demonstration of a functional gripper integrated in the anterior leg. As the gripper comes in contact with a foreign object **(C3)**, an external magnetic force can be used to manipulate the two hands to grab the object **(C4)**. The two hands consist of magnetic particle/polymer composites at their ends that allow for magnetic manipulation. **(D)** The robot uses its frontal gripper to grab an object and then carry it during the process of crawling inside a cylindrical glass pipe with a diameter of 5 mm. **(E)** Schematic and real-life demonstration of the drug reservoir integrated in the anterior leg of the robot. **(F)** The reservoir is covered with a thin layer with a small aperture. **(G, H)** The robot is pushing a small obstacle inside a narrow pipe by converting its body energy. Color images are available online.

Functional gripper and targeted drug delivery application

Along with the ability of multimodal locomotion and excellent adhesive properties, the 3D printed soft robot also has multifunctionality for various bioapplications, including targeted drug delivery and intrabronchial applications such as collecting samples of tissue cells or mucus and removing blockages or foreign bodies from the tracheal and bronchial airways. A frontal gripper and drug-carrying reservoir integrated into the robot body design could enable such applications (Fig. 4C–H). The gripper was integrated into the computer-aided design (CAD) of the soft robot. The whole robot, including the frontal gripper was printed as a monolithic sample in one-platform and one-step directly from the CAD model. Figure 4C1 and C2 shows the CAD model and the printed robot with a gripper integrated. The gripper is composed of functionally gradient nanoparticle/polymer composite. The design strategy is further elaborated in Supplementary Data: Section S3 and the schematic of the gripper design with all dimensions are shown in Supplementary Figures S5 and S6. When the gripper gets in contact with the target object, it converts the magnetic force into mechanical energy and grasps the object until the magnetic force is released. Further details on gripper design are described in Supplementary Data: Section S3. The real-life grabbing experiment is demonstrated in Figure 4D. Additionally, the compliant robot design allows it to conserve a high-potential energy at the maximum bending displacement and then efficiently convert the potential energy to kinetic energy by changing from the maximum bended position (shown in Supplementary Fig. S7a, Pos: 3) to the resting position (Pos: 5) during the crawling locomotion. This added kinetic energy creates a thrust, which also enables the frontal gripper to push obstacles (details of energy conversion strategy of the soft robot is described in Supplementary Data: Section S4). Experiments showed that the robot is able to push an object with a weight ranging from $\sim$0.06 g (0.3 times of robot's weight) to $\sim$1.9 g (8 times of robot's weight) in congested spaces, for example, in the 5 mm diameter glass tubes as shown in Figure 4G and H and the Supplementary Data: Section S4, or gastric folds of moist pig stomach with a controllable high speed (e.g., 8–31 mm/s). The gripping and pushing functionalities of the printed soft robot is demonstrated in Supplementary Movies S3 and S4.

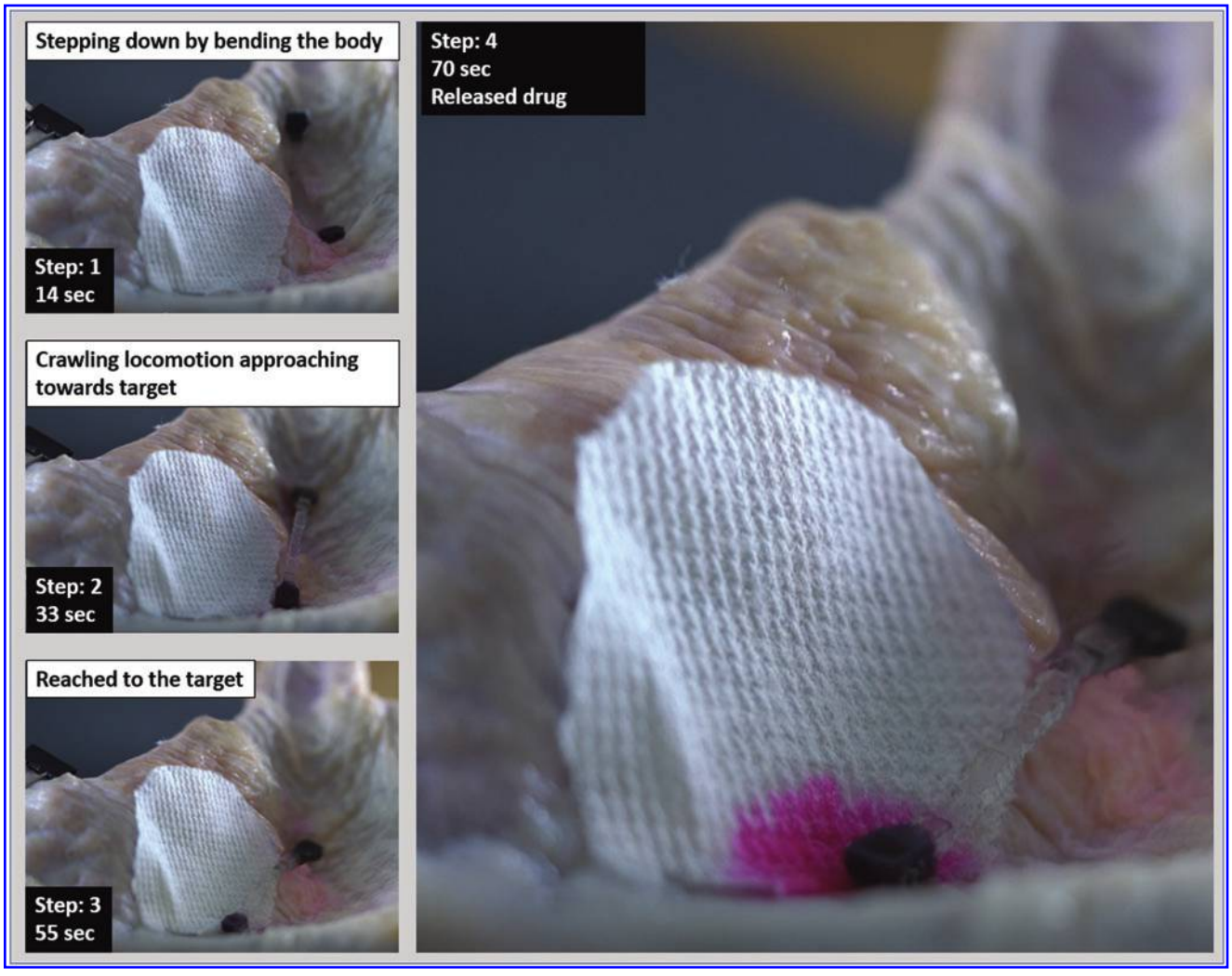

FIG. 5. Demonstration of robot locomotion and drug transportation inside an *in vitro* chicken skin tissue stretched over a human stomach mold. The robot can travel 93 mm of distance (starting point to target) in 70 s in this wet harsh and rough environment. Color images are available online.

As a second test case and potential bioapplication, a targeted drug delivery experiment is demonstrated with the printed soft robot. The robot primarily uses a drug-carrying reservoir in its anterior leg to carry liquid drug to a targeted location. The volume of the drug reservoir is 9.3 mm^3, which is ≈6% of the robot body volume. The drug-carrying reservoir is designed in such a way that it is sealed during locomotion and upon reaching a targeted location the drug is released from a small aperture on the top surface of the reservoir (Fig. 4E, F). During locomotion, when the anterior leg is under the influence of magnetic force, it remains sealed as the bottom skin of the leg is deflected downward. At a targeted location, the anterior leg is released from the magnetic force and the leg's bottom skin creates an upward thrust which ejects the liquid drug from the aperture. Further details about the drug-carrying reservoir and releasing mechanism can be found in our previously published article.[61]

In our previous study,[62] we demonstrated a sample drug delivery experiment on a human stomach model. In this study, the drug delivery experiments were conducted on an *in vitro* moist chicken skin tissue (Fig. 5) and a pig stomach tissue stretched over a human stomach mold (Supplementary Fig. S9).

In the experiment shown in Figure 5, the robot follows several transition points on its way to the targeted location. At first it crawls through the congested and narrow space inside the esophagus. Then it steps down to the inner area of the stomach; the turning locomotion and bending of its body allow it to move in a stable manner so that the liquid drug could be safely stored in the drug reservoir. The gastric folds of the inner area of the stomach are uneven and unstructured. The robot combines the linear and turning locomotion to steer through varied obstacles such as the gastric molds and uneven surfaces to reach the targeted location (93 mm from the starting point) and release the drug. The total time required to complete the drug delivery was measured to be 35 and 70 s with an average speed of 3.3 and 1.3 mm/s in an anatomical human stomach model and on a chicken skin tissue stretched over a human stomach mold, respectively. The robot was slightly slower on the chicken tissue because of the wet and sticky surface. The robot can also carry a solid drug capsule (up to 30 times of its own weight) by pulling it as a load at its posterior leg. A drug delivery experiment was also conducted on an *in vitro* pig stomach. In the drug delivery experiment conducted on the *in vitro* pig stomach (Supplementary Fig. S9), the robot could successfully carry a load and reach to the targeted space with it. The maximum load-carrying capacity of the robot is ∼3 g on slippery and uneven surface like porcine stomach, which is ∼13 times of its body weight (0.23 g) as shown in Supplementary Data (Section S6). The maximum load the robot can carry on a flat surface is ∼7 g, which is ∼30 times of its body weight. Experiments show that the soft robot is robust enough to move on slippery or sticky substrates or crawling in liquids (Fig. 5; Supplementary Figs. S4 and S9; Supplementary Movies S2 and S6).

Feasibility of magnetic actuation strategy in future in vivo *applications*

While our study utilizes the advantages of untethered magnetic actuation for soft robot locomotion, there must be further studies conducted for *in vivo* bioapplications. In our previous study,[57] a simulation analysis was conducted in COMSOL to measure the proper amount of magnetic field strength and magnetic flux density needed to manipulate the robot movement. Furthermore, the thickness of skin and underlying tissues[63] were also considered to be important factors to study before conducting real-life experiments. The locomotion and drug delivery experiments in the stomach model and real pig stomach were done considering the tissue thickness. During the experiment, the distance between the robot legs and the permanent magnets underneath the robot was

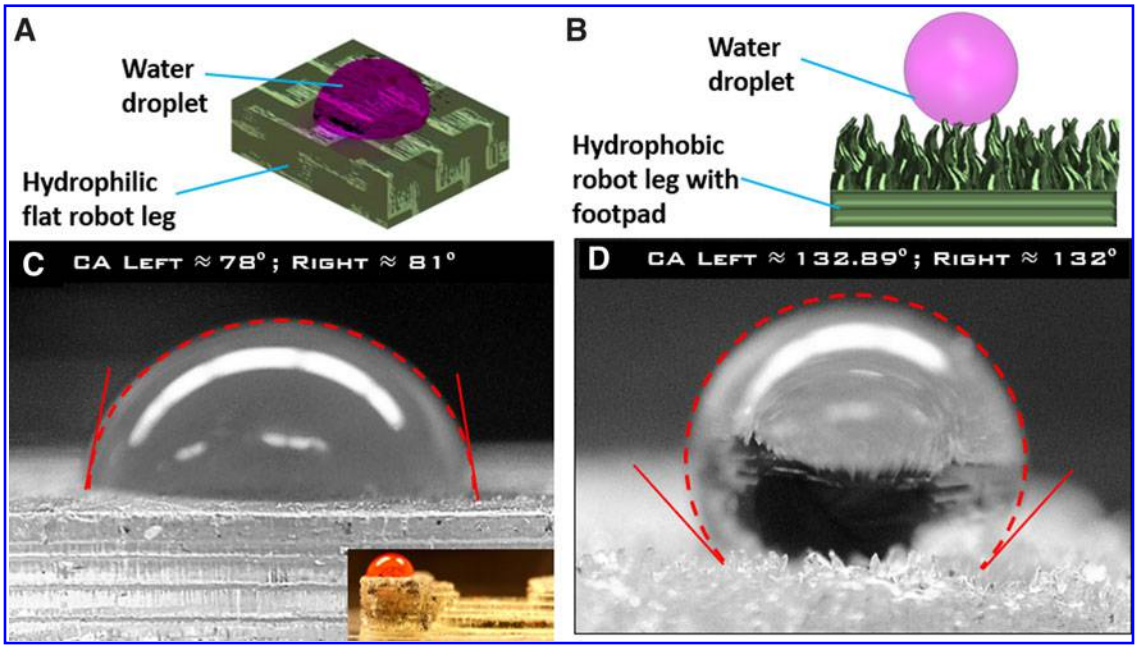

FIG. 6. Robot leg wettability measurement in humid environment. **(A, C)** Water drop on a smooth footpad which has no spike surface structures: contact angle is measured to be ∼78° (*left*) and 81° (*right*). **(B, D)** Water drop on a footpad, which has spike surface structures: contact angle is measured to be ∼132.89° (*left*) and 132° (*right*). Color images are available online.

10 and 30 mm for the stomach model and pig stomach, respectively. The magnetic field strength used for these experiments was 6–7.8 mT. In practical *in vivo* applications, a much stronger magnetic field has to be used if the magnets are placed outside of the body. According to literature,[64] in a controlled environment, magnetic field strengths up to 10 T have been used in *in vivo* research applications (i.e., magnetic resonance imaging), which would be sufficient for external magnetic actuation of the proposed soft robot. However, one potential issue would be preventing magnetic field blending, which might make the individual activation of anterior and posterior legs difficult. A potential solution is to use the same magnetic pole at the two ends of the robot body or use a localized shield to magnify the targeted magnetic field at corresponding legs.

Hydrophobicity caused by the spike surface structure

Generally, a surface is considered hydrophobic when the contact angle is higher than 90°.[65] In addition to a much higher adhesion, the 3D printed spiked footpad attached to the soft robot leg changes the naturally hydrophilic surface to highly hydrophobic (defined by high contact angle $\sim$132°). The footpad covered by spike surface structures allows for low interfacial interaction and surface energy with wet or slippery surfaces. As shown in Figure 6A and C, on a smooth footpad, which has no surface structure, a water droplet creates a contact angle of $\sim$81°. In contrast, the footpad covered by spike surface structure exhibits a much higher contact angle ($\sim$132°), as shown in Figure 6B and D. The tapered shape of the printed spikes combined with a very small contact surface area resulted in hydrophobicity. The relationship between contact angle and the surface area is further discussed in Supplementary Data: Section S1 and the relationship between the contact angle and spike shape is shown in Supplementary Figure S1. From literature, it is known that the hydrophobic property induces higher adhesion forces in wet environments.[27,37,66] This enhances the overall grip and ability of the soft robot to move on various surfaces such as harsh humid environments.

Biocompatibility of robot

From literature,[67,68] it is hypothesized that the unique surface morphology of the footpad is not only responsive to interactions with external stimuli but also has great potential for biosensing due to its ability to adhere with living cells or tissues. Theories were developed to support the hypothesis, yet no experiment validations were presented. In this study, we tested this hypothesis experimentally, by seeding some human umbilical venous endothelial cells (HUVECs) on the spiked footpad at a density of 4000/cm^2 with a passage number of 4. Cells were grown in an incubator at 37°C, with 5% CO_2. Cell cytoplasm was stained by incubating for 30 min with Calcein AM at 1 μm. Calcein shows the viability of living cells, which become fluorescent after hydrolysis by intracellular enzymes. Cells were then imaged using a Zeiss LSM 710 Confocal Microscope at 37°C with 5% CO_2, 6 and 72 h after seeding. Green (Calcein) and blue (material autofluorescence) channels of the images were imported into MATLAB for analysis as individual images. Three-dimensional reconstructions of the cell distribution inside the spiked footpad are shown in Figure 7. Figure 7B and C shows the attached cells (green color) on the spike structure on the footpad surface after 6 and 72 h of seeding, respectively. It shows that the spike surface structure provides a good environment for cell growth. It implies that the soft robot material and its hierarchical surface structure are biocompatible and could provide a good environment for the cells to attach and grow.

Conclusion

In conclusion, this study demonstrates the design, fabrication, and applications of an untethered, multimaterial, and multiscale soft robot, which is composed of spatially varied material compositions and nano- to mm-scale surface features. The multimaterial soft robot is designed with biomimetic footpads covered by hierarchical surface structures, which enable robust multimodal locomotion in dynamic and harsh environments. Multimodal locomotion tasks, such as crawling, turning, and underwater crawling, have been demonstrated through experiments on surfaces with varied wetness and roughness, and harsh environments, including liquid-filled congested glass tubes, complex curly mazes, gastric folds of a human stomach model, and moist animal skin surfaces. With the untethered magnetic actuation and a 3-DOF bending capability, the robot was able to navigate

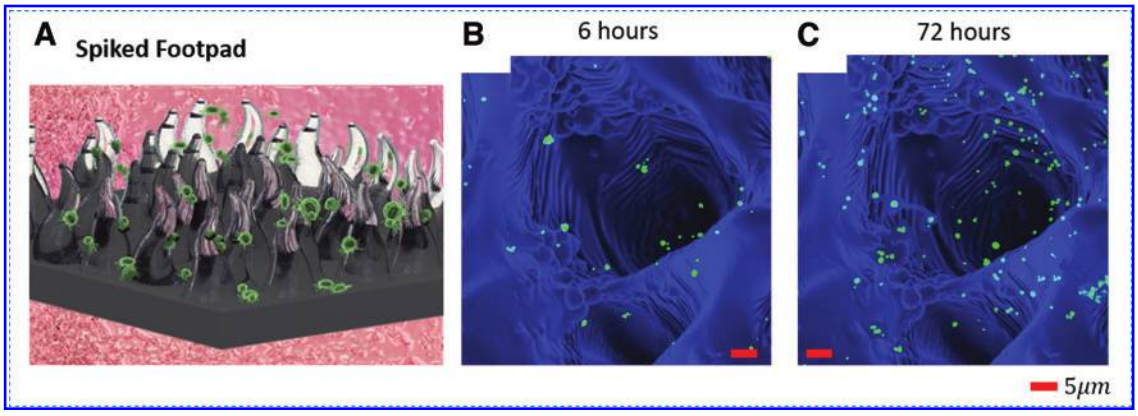

FIG. 7. Biocompatibility test of the printed soft robot. **(A)** Schematic diagram of cell attachment on the robot footpad surface, which is covered by spike structures. **(B, C)** Confocal microscopy images of HUVECs attachment on the footpad: **(B)** Cell culture (*green color*) on the footpad surface (*blue color*) after 6 h of seeding; and **(C)** after 72 h of seeding. HUVEC, human umbilical venous endothelial cell. Color images are available online.

through obstacles, with a locomotion speed in the range of 1.3–3.3 mm/s on different surfaces, a 146° maximum bending angle, a high load-carrying capability (~ 30 times of own body weight), and an efficient obstacle removal ability (e.g., 0.3–8 times of own body weight with a speed as high as 31 mm/s). These functionalities were highly integrated in a single robot, due to its multimaterial designs and multiscale features, including a footpad with hierarchical surface structures, frontal gripper with gradient material distribution, and a liquid drug carrier inside the anterior leg chambers. Moreover, the multimaterial multiscale soft robot demonstrates efficient locomotion and flexibility in integrating with varied functions, which can lead to several applications, such as controlled drug delivery, intrabronchial obstacle removal, and an excellent biocompatible surface, for supporting cell attachment and growth, as demonstrated in the experimental section of this study. The multifunctional soft robot design along with the novel direct digital manufacturing method can greatly benefit the development of powerful, sophisticated, yet easy-to-fabricate soft robots for a wide range of industrial and research applications.

Our future work will focus on conducting validation studies for clinical deployment. Further work is required for enabling closed-loop control of the robot locomotion and release of liquid and solid drug deep in the human body. Experiments must be conducted to test the soft robot *in vivo* in the future. Moreover, biological and pathological studies are also required to test the dynamic and mechanical compatibility of soft robot inside real esophagus and stomach, and how the *in vitro* and *in vivo* tissues respond to delivered therapeutics through the soft robot.

Materials and Methods

Fabrication of multimaterial multiscale soft robot using M-SL

In this study, a novel multimaterial 3D printing process, M-SL developed in our previous articles,[54,56,69] is employed to fabricate the proposed multiscale and multimaterial soft robot. This method can fabricate particle/polymer composite structures directly from the digital model, in a layer-by-layer manner. The M-SL setup design and the developed prototype are shown in Figure 2. The system has an effective light wavelength of 380–420 nm and utilizes a digital micromirror device with a resolution of 1024×768 pixels to pattern light beam with an envelope size of 42.7×32 mm. Further details of the 3D printing process and experiments can be found in our previous publication.[56,69] As the base material for printing the proposed soft robot, Spot E elastic from Spot A Materials (Sonnaya Ulitka S.L., Barcelona, Spain) was used, which allows the cured polymer to bend easily.[57] EMG 1200 dry magnetic nanoparticles (Ferrotec Corporation, NH) with 10 nm nominal particle diameter was used as the magnetic functional particle filler in the proposed soft robot. The EMG 1200 contains 60–80 wt% of iron oxide and has a saturation magnetization of 50–70 emu/g.

To print the proposed soft robot, the designed digital model is first sliced into a set of two-dimensional (2D) layers. Some regions of the sliced 2D layers contain pure polymer, for example, the transparent green robot body region as illustrated in Figure 2A, whereas some regions are made of magnetic particle/polymer composites, such as the two gray-colored legs in Figure 2A. To fabricate a layer with magnetic nanoparticles embedded in desired regions with the designed concentration, a series of magnetic particle distribution operations is performed during the printing process. For example, to fabricate a layer of soft robot with the pure polymer body and the two composite legs, first, a certain amount of magnetic particles is deposited into the resin vat. The magnetic particles are guided to the anterior and posterior leg positions with the help of an external moving magnetic field. The corresponding composite curing mask image of the layer (which is the sliced image of the robot legs) is then projected to the particle filling region, with a carefully calculated projection time. After this composite image curing, another mask image which covers the whole 2D layer area of that layer, is projected to cure the whole 2D layer. The projection time of the second mask image projection is also carefully computed, using the method developed in our previous publication,[54] to ensure printing accuracy. Image projection times for different layer thicknesses and different particle-loading fractions were identified based on the inherent relationship between the curing depth and the material composition.[54]

For the multimaterial soft robot proposed in this study, the weight loading fraction of the magnetic particles in the legs and the gripper regions ranges from 3.64% to 48.93% w/w particles to polymers. The anterior and posterior legs are made of uniform particle/polymer composite with a particle-loading fraction of 48.93 wt%, and hence the composite region of each layer was printed with a single binary image for the leg regions. To print a layer with the gripper which is designed with functionally graded particle/polymer composites (particle-loading fraction gradually increases from 7.39 to 28.55 wt%), a gray-scale mask image is designed to cure the gradient particle/polymer composite region, to achieve a consistent degree of curing and a desired printing accuracy. The gray-scale mask image design is based on the relationship between the gray-scale value and light intensity, as developed in our previous publications.[54,69] After finishing printing a layer, the platform moves up to separate the newly printed layer from the platform and the system continues with the next layer printing until the last layer is finished. The printed soft robot samples are rinsed in alcohol and postcured in an ultraviolet chamber for 20 s to relieve from any remaining residual stress.

Author Contributions

E.B.J. designed and conducted all the experiments, analyzed data, and prepared the article; A.S. conducted cell adhesion experiment, imaging of HUVEC, and helped writing part of the article; D.E. provided advice on cell-adhesion experiments and helped reviewing the article; Y.P. supervised all experiments, data analysis, and article preparation.

Author Disclosure Statement

No competing financial interests exist.

Funding Information

No funding was received for this study.

Supplementary Material

Supplementary Data
Supplementary Figure S1
Supplementary Figure S2
Supplementary Figure S3
Supplementary Figure S4
Supplementary Figure S5
Supplementary Figure S6
Supplementary Figure S7
Supplementary Figure S8
Supplementary Figure S9
Supplementary Figure S10
Supplementary Figure S11
Supplementary Movie S1
Supplementary Movie S2
Supplementary Movie S3
Supplementary Movie S4
Supplementary Movie S5
Supplementary Movie S6

References

1. Kim S, Laschi C, Trimmer B. Soft robotics: a bioinspired evolution in robotics. Trends Biotechnol 2013;31:287–294.
2. Laschi C, Cianchetti M. Soft robotics: new perspectives for robot bodyware and control. Front Bioeng Biotechnol 2014;2:3.
3. Miriyev A, Stack K, Lipson H. Soft material for soft actuators. Nat Commun 2017;8:596.
4. Rus D, Tolley MT. Design, fabrication and control of soft robots. Nature 2015;521:467.
5. Trimmer B. A Journal of Soft Robotics: Why Now? Mary Ann Liebert, Inc.: New Rochelle, NY, 2014.
6. Alapan Y, Yasa O, Schauer O, *et al.* Soft erythrocyte-based bacterial microswimmers for cargo delivery. Sci Robot 2018;3:eaar4423.
7. Yan X, Zhou Q, Vincent M, *et al.* Multifunctional biohybrid magnetite microrobots for imaging-guided therapy. Sci Robot 2017;2:eaaq1155.
8. Zatopa A, Walker S, Menguc Y. Fully soft 3D-printed electroactive fluidic valve for soft hydraulic robots. Soft Robot 2018;5:258–271.
9. Ghosh A, Yoon C, Ongaro F, *et al.* Stimuli-responsive soft untethered grippers for drug delivery and robotic surgery. Front Mech Eng 2017;3:7.
10. Xu H, Sanchez MM, Magdanz V, *et al*. Sperm-hybrid micromotor for drug delivery in the female reproductive tract. ACS Nano 2018;12:327–337.
11. Miyashita S, Guitron S, Yoshida K, *et al*. Ingestible, controllable, and degradable origami robot for patching stomach wounds. 2016 IEEE International Conference on Robotics and Automation (ICRA): IEEE, New York, NY; 2016:909–916.
12. Pfeifer R, Lungarella M, Iida F. Self-organization, embodiment, and biologically inspired robotics. Science 2007; 318:1088–1093.
13. Wang Y, Yang X, Chen Y, *et al.* A biorobotic adhesive disc for underwater hitchhiking inspired by the remora suckerfish. Sci Robot 2017;2:eaan8072.
14. Hu W, Lum GZ, Mastrangeli M, *et al*. Small-scale soft-bodied robot with multimodal locomotion. Nature 2018;554:81.
15. Lin H-T, Leisk GG, Trimmer B. GoQBot: a caterpillar-inspired soft-bodied rolling robot. Bioinspir Biomim 2011; 6:026007.
16. Yim S, Sitti M. Design and rolling locomotion of a magnetically actuated soft capsule endoscope. IEEE Trans Robot 2011;28:183–194.
17. Luo M, Agheli M, Onal CD. Theoretical modeling and experimental analysis of a pressure-operated soft robotic snake. Soft Robot 2014;1:136–146.
18. Luo M, Tao W, Chen F, *et al*. Design improvements and dynamic characterization on fluidic elastomer actuators for a soft robotic snake. 2014 IEEE International Conference on Technologies for Practical Robot Applications (TePRA): IEEE; 2014:1–6.
19. Marchese AD, Katzschmann RK, Rus D. Whole arm planning for a soft and highly compliant 2D robotic manipulator. 2014 IEEE/RSJ International Conference on Intelligent Robots and Systems: IEEE; 2014:554–560.
20. Onal CD, Rus D. Autonomous undulatory serpentine locomotion utilizing body dynamics of a fluidic soft robot. Bioinspir Biomim 2013;8:026003.
21. Rafsanjani A, Zhang Y, Liu B, *et al*. Kirigami skins make a simple soft actuator crawl. Sci Robot 2018;3:eaar7555.
22. Kim Y, Parada GA, Liu S, *et al*. Ferromagnetic soft continuum robots. Sci Robot 2019;4:eaax7329.
23. Lin H-T, Slate DJ, Paetsch CR, *et al*. Scaling of caterpillar body properties and its biomechanical implications for the use of a hydrostatic skeleton. J Exp Biol 2011;214:1194–1204.
24. Wang C, Sim K, Chen J, *et al.* Soft Ultrathin electronics innervated adaptive fully soft robots. Adv Mater 2018;30: 1706695.
25. Vikas V, Cohen E, Grassi R, *et al.* Design and locomotion control of a soft robot using friction manipulation and motor-tendon actuation. IEEE Trans Robot 2016;32:949–959.
26. Hawkes EW, Blumenschein LH, Greer JD, *et al*. A soft robot that navigates its environment through growth. Sci Robot 2017;2:eaan3028.
27. Lu H, Zhang M, Yang Y, *et al.* A bioinspired multilegged soft millirobot that functions in both dry and wet conditions. Nat Commun 2018;9:3944.
28. Morin SA, Shepherd RF, Kwok SW, *et al*. Camouflage and display for soft machines. Science 2012;337:828–832.
29. Wang W, Lee J-Y, Rodrigue H, *et al*. Locomotion of inchworm-inspired robot made of smart soft composite (SSC). Bioinspir Biomim 2014;9:046006.
30. Acome E, Mitchell S, Morrissey T, *et al.* Hydraulically amplified self-healing electrostatic actuators with muscle-like performance. Science 2018;359:61–65.
31. Zhao Y, Wu Y, Wang L, *et al.* Bio-inspired reversible underwater adhesive. Nat Commun 2017;8:2218.
32. Miyashita S, Guitron S, Li S, *et al*. Robotic metamorphosis by origami exoskeletons. Sci Robot 2017;2:eaao4369.
33. Kim S, Spenko M, Trujillo S, *et al*. Smooth vertical surface climbing with directional adhesion. IEEE Trans Robot 2008;24:65–74.
34. Umedachi T, Vikas V, Trimmer B. Softworms: the design and control of non-pneumatic, 3D-printed, deformable robots. Bioinspir Biomim 2016;11:025001.
35. Umedachi T, Vikas V, Trimmer BA. Highly deformable 3-D printed soft robot generating inching and crawling locomotions with variable friction legs. 2013 IEEE/RSJ International Conference on Intelligent Robots and Systems: IEEE, New York, NY; 2013:4590–4595.
36. Yang Y, Chen Z, Song X, *et al.* Biomimetic anisotropic reinforcement architectures by electrically assisted nanocomposite 3D printing. Adv Mater 2017;29:1605750.

37. Yang Y, Li X, Zheng X, *et al*. 3D-printed biomimetic super-hydrophobic structure for microdroplet manipulation and oil/water separation. Adv Mater 2018;30:1704912.
38. Li X, Chen Y. Multi-scale 3D printing of bioinspired structures with functional surfaces. Proceedings of the International Symposium on Flexible Automation: The Institute of Systems, Control and Information Engineers, New York, NY; 2018:13–20.
39. Kim Y, Yuk H, Zhao R, *et al*. Printing ferromagnetic domains for untethered fast-transforming soft materials. Nature 2018;558:274.
40. Diller E, Sitti M. Three-dimensional programmable assembly by untethered magnetic robotic micro-grippers. Adv Funct Mater 2014;24:4397–4404.
41. Kuo J-C, Huang H-W, Tung S-W, *et al*. A hydrogel-based intravascular microgripper manipulated using magnetic fields. Sens Actuators A Phys 2014;211:121–130.
42. Gorb SN, Heepe L. Biological fibrillar adhesives: functional principles and biomimetic applications. In: da Silva LFM, Öchsner A, Adams RD (eds). Handbook of Adhesion Technology. Springer, Berlin, Heidelberg, 2018:1409–1436.
43. Cruz MS, Robles MV, Jespersen JB, *et al.* Scanning electron microscopy of foreleg tarsal sense organs of the poultry red mite, *Dermanyssus gallinae* (DeGeer)(Acari: Dermanyssidae). Micron 2005;36:415–421.
44. Betz O. Adhesive exocrine glands in insects: morphology, ultrastructure, and adhesive secretion. In: von Byern J and Grunwald I (eds). Biological Adhesive Systems. Springer: Elsevier, Vienna; 2010:111–152.
45. Federle W, Riehle M, Curtis AS, *et al*. An integrative study of insect adhesion: mechanics and wet adhesion of pretarsal pads in ants. Integr Comp Biol 2002;42:1100–1106.
46. Gorb SN. The design of the fly adhesive pad: distal tenent setae are adapted to the delivery of an adhesive secretion. Proc Royal Soc Lond Ser B Biol Sci 1998;265:747–752.
47. Gorb SN. Smooth attachment devices in insects: functional morphology and biomechanics. Adv Insect Physiol 2007; 34:81–115.
48. Peattie A, Full R. Phylogenetic analysis of the scaling of wet and dry biological fibrillar adhesives. Proc Natl Acad Sci 2007;104:18595–18600.
49. Spinner M, Westhoff G, Gorb SN. Subdigital setae of chameleon feet: friction-enhancing microstructures for a wide range of substrate roughness. Sci Rep 2014;4:5481.
50. Trimmer B, Issberner J. Kinematics of soft-bodied, legged locomotion in Manduca sexta larvae. Biol Bull 2007;212: 130–142.
51. Van Griethuijsen L, Trimmer B. Locomotion in caterpillars. Biol Rev 2014;89:656–670.
52. Arzt E, Gorb S, Spolenak R. From micro to nano contacts in biological attachment devices. Proc Natl Acad Sci 2003; 100:10603–10606.
53. Tian Y, Pesika N, Zeng H, *et al.* Adhesion and friction in gecko toe attachment and detachment. Proc Natl Acad Sci s 2006;103:19320–19325.
54. Joyee EB, Lu L, Pan Y. Analysis of mechanical behavior of 3D printed heterogeneous particle-polymer composites. Compos Part B Eng 2019.
55. Miller C, Resler Jr E. Magnetic forces and the surface instability in ferromagnetic fluids. Phys Fluids 1975;18: 1112–1118.
56. Joyee EB, Szmelter A, Eddington D, Pan Y. Magnetic field-assisted stereolithography for productions of multimaterial hierarchical surface structures. ACS Appl Mater Interfaces 2020;12:42357–42368.
57. Joyee EB, Pan Y. A fully three-dimensional printed inchworm-inspired soft robot with magnetic actuation. Soft Robot 2019;6:333–345.
58. Leszczynski D. Rapporteur report: cellular, animal and epidemiological studies of the effects of static magnetic fields relevant to human health. Progr Biophys Mol Biol 2005;87:247–253.
59. World Health Organization. Electromagnetic fields and public health. Rev Panamericana Salud Públ 1998;3:206–207.
60. World Health Organization. Environmental Health Criteria 232. Static Fields. Geneva: World Health Organization; 2006.
61. Joyee EB, Pan Y. Multi-material additive manufacturing of functional soft robot. Proc Manuf 2019;34:566–573.
62. Joyee EB, Pan Y. Additive manufacturing of multi-material soft robot for on-demand drug delivery applications. J Manuf Process 2020;56:1178–1184.
63. Hirsch LJ, Strauss KW. The injection technique factor: what you don't know or teach can make a difference. Clin Diabetes 2019;37:227–233.
64. WHO. Electromagnetic fields and public health. https://www.who.int/peh-emf/publications/facts/fs299/en; 2006.
65. Chieng BW, Ibrahim NA, Daud NA, *et al*. Functionalization of Graphene Oxide Via Gamma-Ray Irradiation for Hydrophobic Materials. Synthesis, Technology and Applications of Carbon Nanomaterials. Elsevier, Vienna; 2019: 177–203.
66. Barbieri L, Wagner E, Hoffmann P. Water wetting transition parameters of perfluorinated substrates with periodically distributed flat-top microscale obstacles. Langmuir 2007;23:1723–1734.
67. Li M, Joung D, Hughes B, *et al*. Wrinkling non-spherical particles and its application in cell attachment promotion. Sci Rep 2016;6:30463.
68. Visaveliya NR, Leishman CW, Ng K, *et al.* Surface wrinkling and porosity of polymer particles toward biological and biomedical applications. Adv Mater Interf 2017;4: 1700929.
69. Lu L, Joyee EB, Pan Y. Correlation between microscale magnetic particle distribution and magnetic-field-responsive performance of three-dimensional printed composites. J Micro NanoManuf 2018;6:010904.

Address correspondence to:
Yayue Pan
Department of Mechanical and Industrial Engineering
University of Illinois at Chicago (UIC)
842 W Taylor Street, ERF 1076
Chicago, IL 60607
USA

E-mail: yayuepan@uic.edu